

Ultra-thin electron collectors based on nc-Si:H for high-efficiency silicon heterojunction solar cells

Zhao, Yifeng; Mazzarella, Luana; Procel, Paul; Han, Can; Tichelaar, Frans D.; Yang, Guangtao; Weeber, Arthur; Zeman, Miro; Isabella, Olindo

DOI

[10.1002/pip.3502](https://doi.org/10.1002/pip.3502)

Publication date

2021

Document Version

Final published version

Published in

Progress in Photovoltaics: research and applications

Citation (APA)

Zhao, Y., Mazzarella, L., Procel, P., Han, C., Tichelaar, F. D., Yang, G., Weeber, A., Zeman, M., & Isabella, O. (2021). Ultra-thin electron collectors based on nc-Si:H for high-efficiency silicon heterojunction solar cells. *Progress in Photovoltaics: research and applications*, 30(8), 809-822. <https://doi.org/10.1002/pip.3502>

Important note

To cite this publication, please use the final published version (if applicable).
Please check the document version above.

Copyright

Other than for strictly personal use, it is not permitted to download, forward or distribute the text or part of it, without the consent of the author(s) and/or copyright holder(s), unless the work is under an open content license such as Creative Commons.

Takedown policy

Please contact us and provide details if you believe this document breaches copyrights.
We will remove access to the work immediately and investigate your claim.

Ultra-thin electron collectors based on nc-Si:H for high-efficiency silicon heterojunction solar cells

Yifeng Zhao¹  | Luana Mazzarella¹ | Paul Procel^{1,2}  | Can Han^{1,3}  |
Frans D. Tichelaar⁴ | Guangtao Yang¹ | Arthur Weeber^{1,5} | Miro Zeman¹ |
Olindo Isabella¹

¹Photovoltaic Materials and Devices group, Delft University of Technology, Delft, The Netherlands

²Institute of Micro and Nanoelectronics, San Francisco de Quito University, Quito, Ecuador

³Shenzhen Institute of Wide-bandgap Semiconductors, Shenzhen, China

⁴Kavli Institute of Technology, Quantum Nanoscience, Delft University of Technology, Delft, The Netherlands

⁵TNO Energy Transition, Solar Energy, Petten, The Netherlands

Correspondence

Yifeng Zhao, Photovoltaic Materials and Devices group, Delft University of Technology, Delft, The Netherlands.
Email: y.zhao-4@tudelft.nl

Abstract

Low parasitic absorption and high conductivity enable (*n*)-type hydrogenated nanocrystalline silicon [(*n*)nc-Si:H], eventually alloyed with oxygen [(*n*)nc-SiO_x:H], to be deployed as window layer in high-efficiency silicon heterojunction (SHJ) solar cells. Besides the appropriate opto-electrical properties of these nanocrystalline films, reduction of their thickness is sought for minimizing parasitic absorption losses. Many strategies proposed so far reveal practical limits of the minimum (*n*)-layer thickness that we address and overcome in this manuscript. We demonstrated the successful application of an ultra-thin layer of only 3-nm-thick based on (*n*)nc-Si:H PECVD plasma growth conditions without the use of additional contact or buffer layers. For simplicity, we still name (*n*)nc-Si:H this ultra-thin layer and the solar cell endowed with it delivers a certified efficiency η of 22.20%. This cell shows a 0.61 mA/cm² overall J_{SC} gain over the (*n*)a-Si:H counterpart mainly owing to the higher transparency of (*n*)nc-Si:H, while maintaining comparable $V_{OC} > 714$ mV and $FF > 80\%$. Our optimized (*n*)nc-Si:H layer yields low absorption losses that are commonly measured for (*n*)nc-SiO_x:H films. In this way, we are able to avoid the detrimental effect that oxygen incorporation has on the electrical parameters of these functional layers. Further, by applying a MgF₂/ITO double-layer anti-reflection coating, a cell with 3-nm-thick (*n*)nc-Si:H exhibits a $J_{SC, EQE}$ up to 40.0 mA/cm². By means of EDX elemental mapping, we additionally identified the (*n*)nc-Si:H/ITO interface as critical for electron transport due to unexpected oxidation. To avoid this interfacial oxidation, insertion of a 2-nm-thick (*n*)a-Si:H on the 3-nm-thick (*n*)nc-Si:H contributes to FF gains of 1.4%_{abs.} (FF increased from 78.6% to 80.0%), and showing further room for improvements.

KEYWORDS

(*n*)-type window layers, hydrogenated nanocrystalline silicon, hydrogenated nanocrystalline silicon oxide, opto-electrical properties, ultra-thin (*n*)-contact

This is an open access article under the terms of the Creative Commons Attribution-NonCommercial-NoDerivs License, which permits use and distribution in any medium, provided the original work is properly cited, the use is non-commercial and no modifications or adaptations are made.

© 2021 The Authors. Progress in Photovoltaics: Research and Applications published by John Wiley & Sons Ltd.

1 | INTRODUCTION

Front/back-contacted silicon heterojunction (FBC-SHJ) solar cells with passivating contacts based on hydrogenated amorphous silicon (a-Si:H) have demonstrated conversion efficiency (η) well-above 25%.¹ To reduce the parasitic absorption at the illuminated side, doped a-Si:H is often substituted by doped hydrogenated nanocrystalline silicon (nc-Si:H) and/or its oxygen alloy (nc-SiO_x:H) that concurrently enable better transparency and higher conductivity.^{2–9} These advantageous opto-electrical properties of nc-Si:H-based thin-films mainly originate from their mixed-phase compositions, which consist of nanocrystals embedded in the amorphous matrix.^{10,11}

However, nc-Si:H-based thin-films feature thickness- and substrate-dependent growth characteristics.^{12,13} Thus, efforts have been devoted to minimizing the thickness of the initial amorphous incubation layer regardless of the influence from the substrate. For instance, applying a CO₂ plasma treatment,^{14,15} employing a non-oxidic doped/non-doped seed layer and/or a contact layer,^{3,15–20} using a very-high-frequency (VHF) plasma,^{21,22} utilizing a phosphorous treatment,²³ and implementing a hydrogen plasma treatment²⁴ or a low-temperature crystallization by hydrogen plasma^{25,26} were reported. Such approaches can accelerate the nucleation of nanocrystals, thus enabling doped layers with low activation energies (E_a). And those low values of E_a are critical for effective carrier-selective transport through nc-Si:H-based carrier-selective contacts (CSCs) in SHJ solar cells, which feature (i)a-Si:H passivating layers.²⁷ Besides, prompt nucleations also provide the possibility to minimize the total thicknesses of the nc-Si:H-based CSCs which results in a lower parasitic absorption while maintaining advantageous electrical properties, especially, when they are located on the illuminated side of the solar cells. As reported, for rear junction SHJ solar cells that feature a (n)nc-Si:H-based window layer, the thickness of this (n)nc-Si:H layer should generally be at least around 10-nm to achieve a decent FF of above 77%.^{19,22} For a (n)nc-SiO_x:H-based contact, a minimum of approximately 8-nm-thick (n)-type nc-SiO_x:H in addition to a nc-Si:H layer stack, which acts as a seed and/or contact layer, is needed to form effective electron CSCs for ensuring excellent electrical cell performance including preserving the passivation quality.^{16,28} Attempts for further reducing the nc-Si:H-based (n)-contacts' thicknesses have so far resulted in losses of both FF and V_{OC} of the solar cells.^{19,28,29} Despite this limited thickness, the rather slow deposition rates of nc-Si-based thin films as compared to a-Si:H³ also impose challenges for their industrial feasibility. Therefore, the development of a thin (n)-contact that preserves the electrical performance of solar cells is of great interest for reducing the parasitic absorption by lowering material consumption and enabling higher industrial throughputs.

In this study, we aim at minimizing the parasitic absorption of the (n)-type window layers while keeping excellent electrical performances. We investigated and compared the opto-electrical properties of (n)a-Si:H, (n)nc-SiO_x:H and (n)nc-Si:H layers and their performances (as thin as 2 nm) in rear junction FBC-SHJ solar cells. By means of our hydrogen plasma treatment (HPT) and VHF (i)nc-Si:H treatment, we demonstrated the successful application of an ultra-thin layer of only

3-nm-thick based on (n)nc-Si:H PECVD plasma growth conditions without the use of additional contact or buffer layers that delivers a certified conversion efficiency (η) of 22.20%. Furthermore, for understanding the interfacial properties of thin (n)-layers and their effect on the solar cell output parameters, we performed high-resolution transmission electron microscopy (HRTEM) measurements and energy-dispersive X-ray (EDX) elemental mapping analyses.

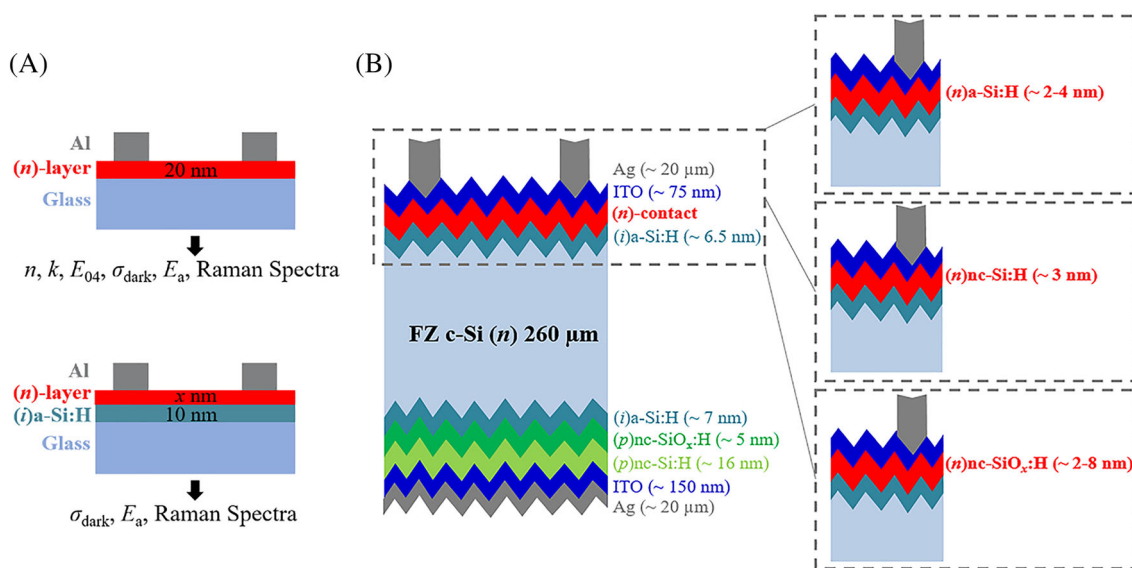
2 | EXPERIMENTAL DETAILS

In this study, thin-film silicon layers were deposited via a multi-chamber plasma-enhanced chemical vapor deposition (PECVD) tool (Elettrovava S.p.A.) that operates at the radio-frequency (RF, 13.56 MHz) or VHF (40.68 MHz). The PECVD deposition conditions that were adjusted to obtain various (n)-type layers are listed in Table 1. More detailed descriptions of the other PECVD deposition conditions can be found in our previous study.³⁰ Specifically, to characterize the optical and electrical properties of different (n)-type layers, two sample configurations were used. For the first configuration, (n)-type layers with a thickness of approximately 20 nm were directly deposited on Corning Eagle XG glasses. For the second configuration and to simulate the actual structure in solar cells, 5- to 20-nm-thick (n)-type layers were deposited on 10-nm-thick (i)a-Si:H coated the same type of glasses. The (i)a-Si:H coated glasses were prepared with consideration of our actual solar cell structure, where (n)-type layers are deposited on (i)a-Si:H passivating layer. The schematic sketches of sample structures are given in Figure 1A. Spectroscopic ellipsometry (SE) (M-2000DI system, J.A. Woollam Co., Inc.) was used to check the thicknesses of deposited layers and to extract the refractive index (n), the extinction coefficient (k) and the optical bandgap (E_{04}). To obtain the dark conductivity (σ_{dark}) at 25°C and the E_a , (n)-type layers that feature 300-nm-thick thermally evaporated Al stripes were measured via a temperature-controlled dark current–voltage (I - V) setup with Keithley 6512B electrometer. The σ_{dark} is defined as the lateral dark conductivity measured for the (n)-layer or (n)-layer/(i)a-Si:H stack divided by the thickness of the (n)-layer. Raman spectroscopy (Renishaw inVia Raman Microscope equipped with a green laser, $\lambda_{\text{laser}} = 514$ nm) was used to characterize the microstructures of (n)-type thin films, which were also used for extracting their optical properties as previously mentioned.

For solar cells fabrication, we used 4-inch (n)-type Topsil float-zone (FZ) <100> c-Si wafers that are 280 ± 20 - μm -thick and have a resistivity of 3 ± 2 $\Omega\cdot\text{cm}$. Prior to the PECVD process, c-Si wafers were randomly textured in diluted tetramethylammonium hydroxide (TMAH) solution with ALKA-TEX as an additive,³¹ subsequently cleaned by sequentially dipping them into 99% nitric acid (HNO₃), 69.5% HNO₃, and lastly 0.55% hydrofluoric acid (HF). After loading the wafers into PECVD, the (i)a-Si:H/(n)-contact stack was firstly deposited. After a short vacuum break, the wafers were flipped and loaded back to PECVD for (i)a-Si:H/(p)nc-SiO_x:H/(p)nc-Si:H depositions. Afterwards, RF magnetron sputtering (Polyteknik AS) was used

TABLE 1 PECVD parameters for optimized (n)nc-SiO_x:H, (n)nc-Si:H, HPT, VHF (i)nc-Si:H treatments

PECVD parameters	(n)a-Si:H	(n)nc-Si:H	(n)nc-SiO _x :H-1	(n)nc-SiO _x :H-2	HPT	VHF (i)nc-Si:H
Frequency (MHz)	13.56	13.56	13.56	13.56	13.56	40.68
Temperature (°C)	180	180	180	180	180	180
Pressure (mbar)	0.6	2.7	1.5	2.7	2.7	4
Power density (mW/cm ²)	28	76	76	76	63	69
SiH ₄ (sccm)	40	1	1	1	/	1.2
H ₂ (sccm)	/	100	100	100	200	120
CO ₂ (sccm)	/	/	1.6	1.6	/	/
PH ₃ (2% in H ₂) (sccm)	11	1.2	1.2	1.2	/	/

**FIGURE 1** Schematic sketches of (A) sample structures to extract n , k , E_{04} , σ_{dark} , E_a and Raman spectra of (n)-type layer; and (B) rear junction FBC-SHJ solar cells with different (n)-layers stacks studied, namely, (n)a-Si:H, (n)nc-Si:H and (n)nc-SiO_x:H [Colour figure can be viewed at wileyonlinelibrary.com]

to deposit-through-mask indium tin oxide (ITO) on the front and rear sides of solar cell precursors with thicknesses of 75 and 150 nm, respectively. The ITO sputtering process was done at a substrate temperature of 105°C. Eventually, Ag screen-printing was applied to form the metal electrodes on both sides of the devices. A paste curing step at 170°C for 45 min in air atmosphere was performed in an oven. Solar cells fabricated in this study have an area of 3.92 cm². The schematic sketches of manufactured solar cells are illustrated in Figure 1B.

Along with the fabrication process of solar cells, the implied- V_{OC} (i - V_{OC}) of solar cell precursors were measured before and after the ITO sputtering by using Sinton WCT-120 with either quasi-steady-state photoconductance (QSSPC) mode or transient photoconductance decay (Transient PCD) mode. Solar cells' external parameters were characterized by using a AAA class Wacom WXS-90S-L2 under standard-test-conditions (STC). An in-house external-quantum-efficiency (EQE) measurement setup was used to analyze the wavelength-dependent spectral response of solar cells without influence from the front metal grids and obtain the integrated $J_{\text{SC,EQE}}$.

Meanwhile, the reflectance (R) of solar cells was measured by PerkinElmer Lambda 1050 system. The independent certifications of solar cells' current-voltage (I - V) characteristics were carried out at the CaTeC of the Institute for Solar Energy Research Hamelin (ISFH), Germany. For HRTEM and EDX analysis of fabricated solar cells, a FEI cubed Cs-corrected Titan was used, operating at 300 kV. EDX maps were obtained using the 4 detector ChemiSTEM of Thermo Fisher. Ray-tracing Genpro4 optical simulations³² with inputs from SE-characterized n and k of Si thin films and ITO were performed for our fabricated double-side-textured SHJ solar cells.

3 | RESULTS AND DISCUSSIONS

3.1 | Opto-electrical properties and Raman spectra of (n)a-Si:H, (n)nc-SiO_x:H and (n)nc-Si:H

The opto-electrical properties of optimized (n)a-Si:H, (n)nc-SiO_x:H and (n)nc-Si:H are shown and compared in Figure 2 and Table 2.

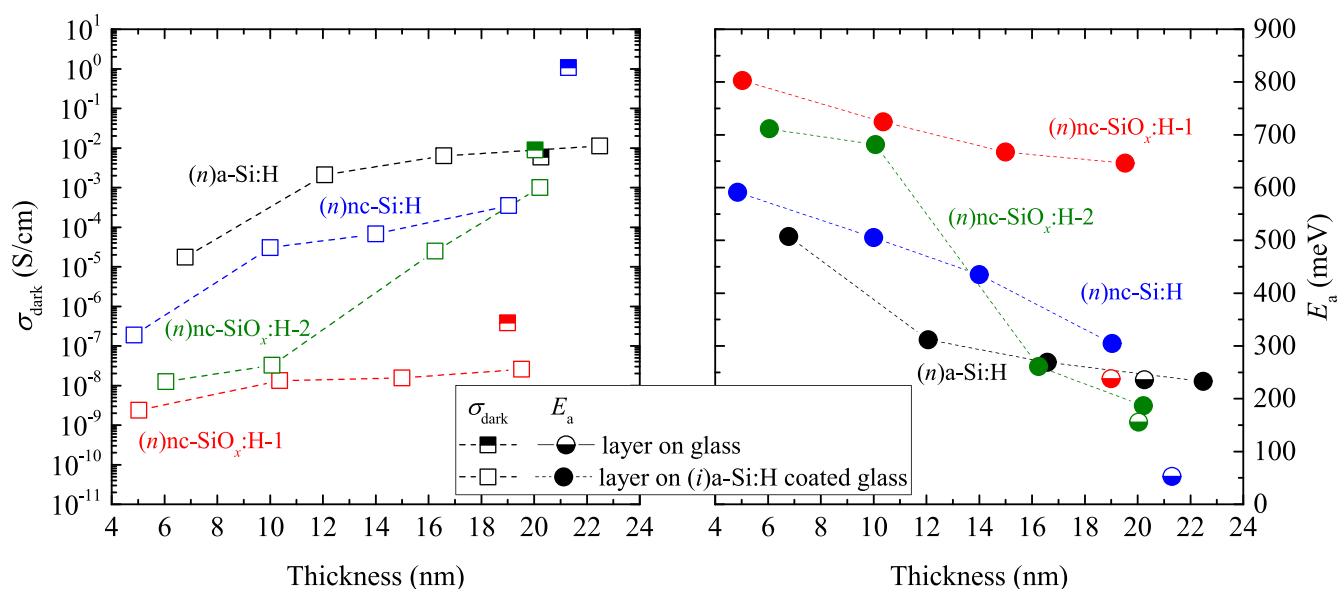


FIGURE 2 The σ_{dark} (left) and E_a (right) of $(n)\text{nc-SiO}_x\text{:H}$, $(n)\text{nc-Si:H}$ and $(n)\text{a-Si:H}$ layers as function of layer thickness and of the different substrates [Colour figure can be viewed at wileyonlinelibrary.com]

TABLE 2 Opto-electrical properties of optimized $(n)\text{a-Si:H}$, $(n)\text{nc-SiO}_x\text{:H}$ and $(n)\text{nc-Si:H}$

Layers	Deposition rate ^a (nm/s)	n @ $\lambda = 632$ nm (-)	E_{04} @ ~ 20 nm (eV)	σ_{dark} @ ~ 20 nm (S/cm)	σ_{dark}^b @ ~ 20 nm (S/cm)	σ_{dark}^b @ ~ 5 nm (S/cm)
$(n)\text{a-Si:H}$	0.101	4.16	1.86	5.9×10^{-3}	1.1×10^{-2}	1.8×10^{-5}
$(n)\text{nc-SiO}_x\text{:H-1}$	0.031	2.08	2.60	3.8×10^{-7}	2.6×10^{-8}	2.4×10^{-9}
$(n)\text{nc-SiO}_x\text{:H-2}$	0.023	2.60	2.26	8.9×10^{-3}	9.9×10^{-4}	1.3×10^{-8}
$(n)\text{nc-Si:H}$	0.027	3.25	1.95	1.07	3.5×10^{-4}	1.9×10^{-7}

^aDeposition rates were calculated based on the measured thin-film thicknesses and their deposition time.

^bLayers were deposited on 10-nm-thick $(i)\text{a-Si:H}$ coated glasses.

Electrically, as illustrated in Figure 2, around 20-nm-thick $(n)\text{nc-Si:H}$ that was deposited on glass substrate shows the highest σ_{dark} of 1.07 S/cm and the lowest E_a of 52.6 meV. This is due to its higher crystalline fraction thus enabling higher doping efficiency as revealed later with Raman spectroscopy. However, the σ_{dark} drops to 3.5×10^{-4} S/cm and the E_a increases to 304.4 meV when $(n)\text{nc-Si:H}$ was deposited on $(i)\text{a-Si:H}$ coated glass substrate. Similarly, substrate-dependent σ_{dark} and E_a are observed for both $(n)\text{nc-SiO}_x\text{:H}$ films. This substrate-dependent growth characteristic is known for nc-Si:H-based thin films.^{12,13,15,33} Ultimately, by thinning all layers down to around 5 nm, which is close to the thickness of (n) -contact in solar cells, $(n)\text{a-Si:H}$ results to be the most conductive, followed by $(n)\text{nc-Si:H}$, $(n)\text{nc-SiO}_x\text{:H-2}$, and $(n)\text{nc-SiO}_x\text{:H-1}$. As it will be discussed later, the higher σ_{dark} and generally lower E_a of $(n)\text{a-Si:H}$ could be attributed to its deposition conditions and its different doping properties from the amorphous incubation phase of nc-Si:H-based films. Moreover, we observed thickness-dependent σ_{dark} and E_a not only for $(n)\text{nc-SiO}_x\text{:H}$ and $(n)\text{nc-Si:H}$ layers, but also for $(n)\text{a-Si:H}$ layers. That is, a thicker

layer exhibits a higher σ_{dark} and a lower E_a . It is known for nc-Si:H-based layers that the evolution of their nanocrystals results in improved electrical properties.¹² While for $(n)\text{a-Si:H}$, the thickness-dependent σ_{dark} and E_a could be ascribed to the non-coalesced films during their initial stage of layers growth,³⁴ which result in reduced material densities thus may negatively affect their electrical properties. Nevertheless, thickness-dependent electrical properties were also reported previously for $(n)\text{a-Si:H}$ thicker than around 100 nm,^{35,36} and those were ascribed to the existence of a resistive surface layer when the layer becomes thin.

As listed in Table 2, $(n)\text{a-Si:H}$, which features the highest n and the lowest E_{04} is optically the least favorable among those (n) -layers. It will be better to make $(n)\text{nc-Si:H}$ and $(n)\text{nc-SiO}_x\text{:H-2}$ layers, while $(n)\text{nc-SiO}_x\text{:H-1}$ features the lowest n of 2.08 and the largest E_{04} of 2.60 eV. The larger E_{04} of nc-Si:H as compared to $(n)\text{a-Si:H}$ could be ascribed to the formation of small Si nanocrystals embedded in $(n)\text{a-Si:H}$ matrix, where the quantum size effect of nanocrystals,³⁷ higher H-incorporation into the amorphous matrix³⁸ or higher void fraction³⁴

may play a role. Despite the aforementioned possible explanations for (n)nc-Si:H, the incorporation of oxygen into the amorphous matrix further widens the E_{04} of both (n)nc-SiO_x:H layers.³⁹ In particular, a higher fraction of oxygen incorporation could account for the higher E_{04} of (n)nc-SiO_x:H-1 as compared to (n)nc-SiO_x:H-2. The n and k of various (n)-type thin films as function of wavelength are provided in Figure S1.

To further correlate the opto-electrical properties of various (n)-type thin films to their microstructural properties, we measure Raman spectra of various (n)-type thin films deposited on top of bare glasses and the ones on 10-nm-thick (i)a-Si:H coated glasses as reported in Figure 3.

As illustrated in Figure 3A, where layers are deposited directly on glass substrates, both nc-Si:H and (n)nc-SiO_x:H-2 exhibit distinguishable Raman peaks near 520 cm⁻¹, which is characteristic of crystalline Si.⁴⁰ This evidences the existence of Si nanocrystals in the films, although those crystalline Si peaks slightly downshift to around 510 cm⁻¹, which is an indication of rather small-size Si nanocrystals in our deposited 20-nm-thick films^{41–43} and/or the tensile strain effect of Si nanocrystals.⁴⁴ It is worth noting that those crystalline Si peaks are also superimposed on a broad amorphous Si peak centered at 480 cm⁻¹,⁴⁵ which suggests the coexistence of amorphous and nanocrystal phases in those films. Nevertheless, the existence of Si nanocrystals in (n)nc-Si:H and (n)nc-SiO_x:H-2 enables better a doping efficiency than amorphous Si,^{46–49} explaining their relative higher σ_{dark} and lower E_a as reported in Figure 2. However, (n)nc-SiO_x:H-2 exhibits a slightly lower σ_{dark} as compared to (n)nc-Si:H due to oxygen incorporation, which results in a weakened doping efficiency.⁵⁰ On the other hand, the (n)nc-SiO_x:H-1 layer reveals a lower fraction of Si nanocrystals, which could be ascribed to the excessive oxygen incorporation, suppressing the growth of nanocrystals.^{51–54} This observation also explains the highest E_{04} and the lowest σ_{dark} obtained for (n)

nc-SiO_x:H-1. As expected, only a broad amorphous Si peak was observed for (n)a-Si:H.

When equivalent-thick 20 nm (n)-type thin films were deposited on (i)a-Si:H coated glasses, all layers appear to be nearly fully amorphous as shown in Figure 3B. This is probably due to the green laser used for Raman spectra, whose penetration depth is in the range of hundreds of nanometers. Thus, the non-negligible signals from the 10-nm-thick (i)a-Si:H coatings may overwhelm the signals from those tiny crystals.⁵⁵ Nevertheless, those nc-Si:H-based layers are amorphous-phase-dominant as nanocrystals are yet to be well-developed to promote higher σ_{dark} or lower E_a than that of the standard (n)a-Si:H. This is because the initial amorphous incubation phase of nc-Si:H-based layer might feature different doping efficiency from that of the standard (n)a-Si:H. As known from the secondary-ion-mass spectroscopy studies for thin (p)nc-Si:H (< 10 nm) and standard (p)a-Si:H by Umishio et al.,⁵⁵ we attribute our observations of higher σ_{dark} and generally lower E_a for the (n)a-Si:H than nc-Si:H-based layers to the following reasons: (a) the nearly 10 times higher flow of doping gas (PH₃) for (n)a-Si:H that can contribute to a higher phosphorous content in (n)a-Si:H, (b) the probably higher phosphorous incorporation efficiency under the deposition conditions of (n)a-Si:H, and (c) a lesser significant dopant inactivation induced by the hydrogen passivation in (n)a-Si:H than in those nc-Si:H-based layers.^{56–58}

As for thickness-dependent σ_{dark} and E_a , for all nc-Si:H-based films, we suspect that the trends should be still related to the nucleation and growth of nanocrystals despite having observed broad amorphous peaks in Raman spectra obtained by the green laser. This assumption is reasonable as for (n)nc-Si:H and (n)nc-SiO_x:H-2 thicker than 15 nm there are steeper slopes of variations of σ_{dark} and E_a than that of the standard (n)a-Si:H (see Figure 2). This suggests an improved doping efficiency with higher fractions of nanocrystals when layers get thicker. Especially, (n)nc-SiO_x:H-2 layers thicker than

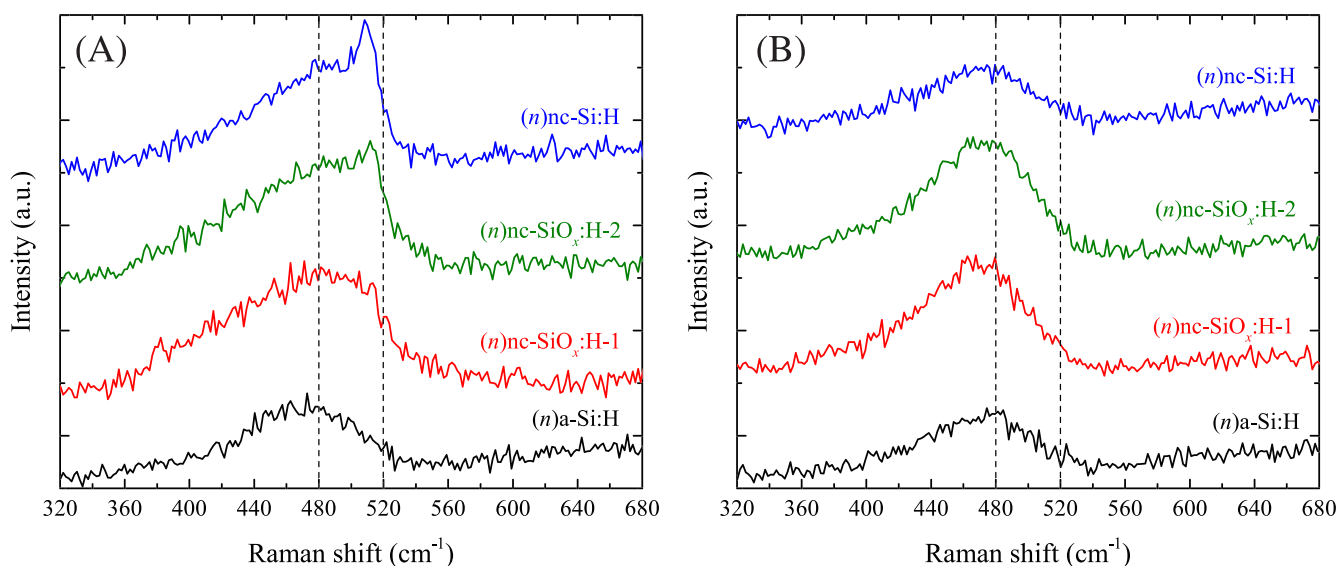


FIGURE 3 Raman spectra of various (n)-type thin films that were deposited on top of the (A) glass substrate, and (B) 10-nm (i)a-Si:H coated glass substrate. Dashed vertical lines indicate the Raman shift of 480 cm⁻¹ and 520 cm⁻¹. Schematic sketches of sample structures are shown in Figure 1A. The thicknesses of deposited (n)-type thin films are around 20 nm [Colour figure can be viewed at wileyonlinelibrary.com]

15 nm have already demonstrated a lower E_a than that of the standard (*n*)a-Si:H (see Figure 2). To further reveal the nanocrystalline fractions in those layers, an ultraviolet laser should be implemented.⁵⁵

3.2 | Solar cells—Various (*n*)-type window layers ≤ 8 nm

Based on the opto-electrical and microstructural properties of various (*n*)-type thin films, we fabricated rear junction FBC-SHJ solar cells as sketched in Figure 1B. Before the depositions of (*n*)-contacts, we also applied previously optimized combined HPT + VHF (*i*)nc-Si:H treatments,³ which have negligible effects on the σ_{dark} for all (*n*)-type layers with thicknesses around 5 nm (see Figure S2). In this section, we compare the performance of solar cells featuring various single-layer (*n*)-contacts (i.e., without additional contact or buffer layers) with different thicknesses. Based on previous optimizations, the 3-nm-thick (*n*)nc-Si:H is chosen as it is the minimum thickness that can already deliver good V_{OC} and FF (see Figure S3). The J - V parameters of solar cells are given in Figure 4.

First, as shown in Figure 4A, we discuss the effect of the ITO sputtering on the passivation quality of cell precursors with different window layers, which are represented by the i - V_{OC} with and without the ITO. Within the thickness range investigated, we observed i - V_{OC} drops of around 10–19 mV for all cell precursors with less conductive (and high E_a) (*n*)nc-SiO_x:H-1. In comparison, the use of 3 nm and 8 nm (*n*)nc-SiO_x:H-2 shows much-lower i - V_{OC} degradations and even improved i - V_{OC} , respectively. We ascribe this to the thickness-dependent σ_{dark} and E_a (see Figure 2), and the stronger capability of more conductive (and a lower E_a) (*n*)nc-SiO_x:H-2 to preserve the field-effect passivation after the ITO sputtering as compared to (*n*)nc-SiO_x:

H-1. We observed a nearly 10 mV i - V_{OC} degradation for cell precursors with 3-nm-thick (*n*)nc-Si:H. Notwithstanding this 3-nm-thick (*n*)nc-Si:H might have a higher σ_{dark} and a lower E_a than that of 8-nm-thick (*n*)nc-SiO_x:H-2 as expected from Figure 2, this degradation could be attributed to the too-thin thickness and seemingly porous structure of this (*n*)nc-Si:H that makes it less robust to sputtering damages as will be discussed later in Section 3.3. Despite the comparisons among different (*n*)-contacts, cell precursors with the same type but a thicker (*n*)-contact showed better passivation resilience against the ITO sputtering as compared to the thinner counterparts.

Besides, we observed significant degradations from i - V_{OC} to V_{OC} after cell metallizations with both (*n*)nc-SiO_x:H thinner than 5 nm as seen in Figure 4A. For instance, although cells with 2- to 4-nm (*n*)nc-SiO_x:H-1 exhibit comparable i - V_{OC} of around 705 mV before metallization, the loss from i - V_{OC} to V_{OC} increases for cells with the thinner (*n*)nc-SiO_x:H-1. We linked those larger losses to the insufficient selectivity and increased recombinations, which seem to be related to the thickness-dependent σ_{dark} and E_a of (*n*)-contacts as shown in Figure 2.²⁷ Nevertheless, cells with 8-nm-thick (*n*)nc-SiO_x:H-1 show the minimum i - V_{OC} to V_{OC} drops among the (*n*)nc-SiO_x:H-1 thickness series. Similar observations were found for cells with (*n*)nc-SiO_x:H-2 and (*n*)a-Si:H where a thicker (*n*)-contact accounts for lesser i - V_{OC} to V_{OC} degradations. Those trends were also found before by Wernerus et al. for both (*n*)nc-Si:H and (*n*)a-Si:H in rear junction SHJ solar cells.³⁴ Therefore, around 8 nm of (*n*)nc-SiO_x:H single-layer is at least required for preserving the passivation quality while being capable of effective electron collections.^{16,28} Despite the i - V_{OC} losses after ITO and metallization for the 3-nm-thick (*n*)nc-Si:H, mainly thanks to its high i - V_{OC} of 745 mV (before ITO sputtering) achieved for cell precursors, the completed solar cells can still exhibit a good V_{OC} of around 719 mV. This high

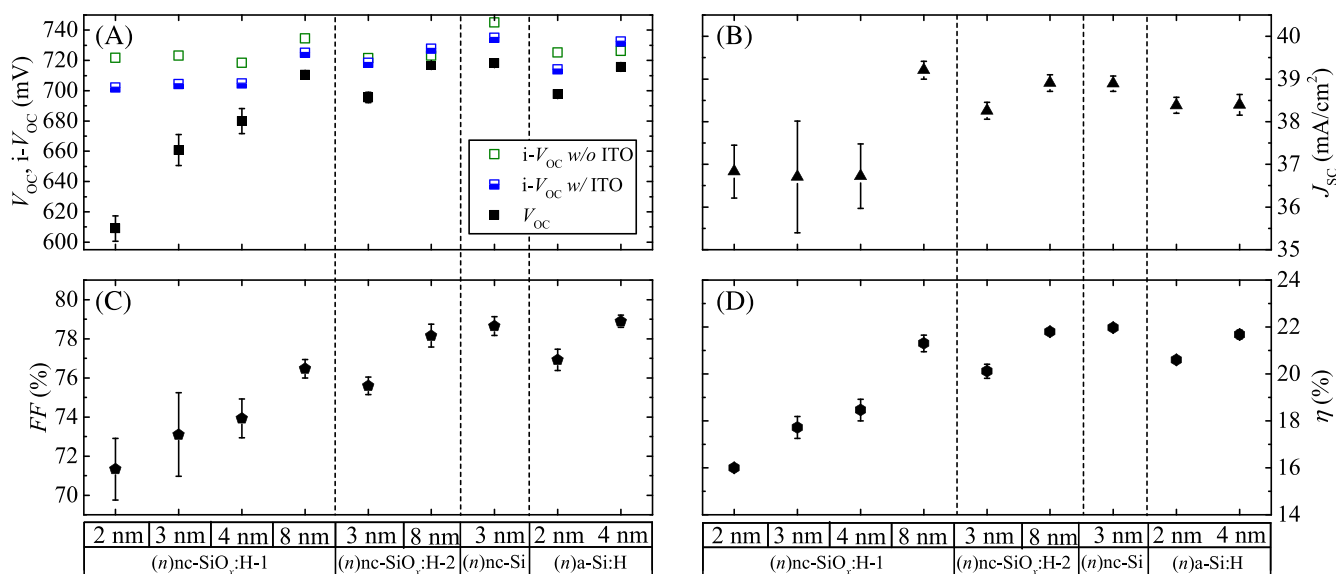


FIGURE 4 The J - V characteristics of rear junction FBC-SHJ solar cells with various (*n*)-type contacts: (A) i - V_{OC} and V_{OC} , (B) J_{SC} , (C) FF , and (D) η . The results represent averaged parameters of four solar cells (3.92 cm²) and the error bars represent the standard deviations [Colour figure can be viewed at wileyonlinelibrary.com]

i - V_{OC} could be attributed to beneficial hydrogen incorporations during the deposition of (n)nc-Si:H layers.^{55,59}

Then as illustrated in Figure 4B,C, cells with both 8-nm-thick (n)nc-SiO_x:H tend to exhibit recovered J_{SC}^{29} and higher $FF^{27,28,60}$ values as compared to their thinner counterparts. Those variations can again be related to the thickness-dependent σ_{dark} and E_a trends as seen in Figure 2. Specifically, the recovered J_{SC} values result from the reduced recombinations and improved selective transport of electrons, which are also suggested by the improved V_{OC} values (see also Figure S4). And for well-passivated cells ($V_{OC} > 710$ mV), the J - V characteristics of solar cells correspond well to the optical properties of (n)-layers and electrical properties of around 5-nm-thick layers as summarized in Table 2. In other words, (n)-layer with a higher σ_{dark} (lower E_a) or a larger E_{04} tends to deliver a higher FF^{27} or J_{SC} in the solar cell, respectively. Thus, cells with (n)a-Si:H demonstrate the highest average FF of 78.9% while cells with 8-nm-thick (n)nc-SiO_x:H-1 exhibit the highest average J_{SC} of 39.2 mA/cm². However, both of their η are slightly limited by the non-optimal tradeoff between the optical and electrical properties of the (n)-contacts. Interestingly, cells with only 3-nm-thick (n)nc-Si:H features not only a favored average J_{SC} of 38.9 mA/cm² but also decent average FF of 78.6% and V_{OC} of 719 mV, thus the highest average η of 22.0% was achieved.

Note that this 3-nm-thick (n)nc-Si:H (n)-contact is expected to feature a high E_a value of at least around 590 meV (see Figure 2) and yet, the corresponding solar cells deliver decent FF s above 78.6% (see Figure 4). Notwithstanding the limited active doping, in such a thin Si layer, the electrons are able to tunnel directly from (n)c-Si to TCO, making the transport of electrons less sensitive to the condition of (n)-contact/TCO heterointerface after processing. Therefore, electrons can be collected effectively as long as the passivation quality is well-preserved. In the case of thicker layers, a similar transport path also happens if the nc-Si:H-based (n)-contacts feature well-developed nanocrystals⁶¹ and special processing condition of (n)-contact/TCO

interface.³ However, the parasitic absorption of thick (n)-contacts will limit the solar cell efficiency. Nevertheless, (n)-contact with a low E_a still benefits the effective collections of electrons.²⁷ Thus, a combination of thinner (n)-contacts exhibiting low E_a is promising to boost the conversion efficiency of solar cells.

The EQE, 1-R spectra and IQE spectra of cells with 8-nm-thick (n)nc-SiO_x:H (both types), 3-nm-thick (n)nc-Si:H and 4-nm-thick (n)a-Si:H are plotted in Figure 5.

As shown in Figure 5A, the differences among various EQE spectra were mainly found in the wavelength range from 300 to 600 nm. In this wavelength range, compared to the cell with (n)a-Si:H, the (n)nc-SiO_x:H-1 cell exhibits a $J_{SC,EQE}$ gain of 0.8 mA/cm², while both (n)nc-SiO_x:H-2 and (n)nc-Si:H counterparts show $J_{SC,EQE}$ improvements of around 0.6 mA/cm². Those EQE differences once more correspond well to the reported optical properties of the (n)-layers as given in Table 2. Specifically, the derived IQE spectra in Figure 5B further reveal the dominant role of parasitic absorptions of various (n)-type window layers on those EQE differences.² This finding is also confirmed by performing optical simulations of our solar cells (see Figure S5). Although the cell with 8-nm-thick (n)nc-SiO_x:H-1 showed the highest integrated $J_{SC,EQE}$ of 39.3 mA/cm², the device with 3-nm-thick (n)nc-Si:H delivered a comparable $J_{SC,EQE}$ of 39.2 mA/cm² thanks to the ultra-low thickness of the (n)-contact. Those results suggest that this 3-nm-thick (n)nc-Si:H is an optically promising window layer for FBC-SHJ solar cells.

3.3 | Solar cells—HRTEM and EDX elemental mapping

We further conducted HRTEM with EDX elemental mapping to investigate: (a) the thickness of (n)-type layers deposited; (b) the microstructural characteristics of various (n)-type films deposited in solar

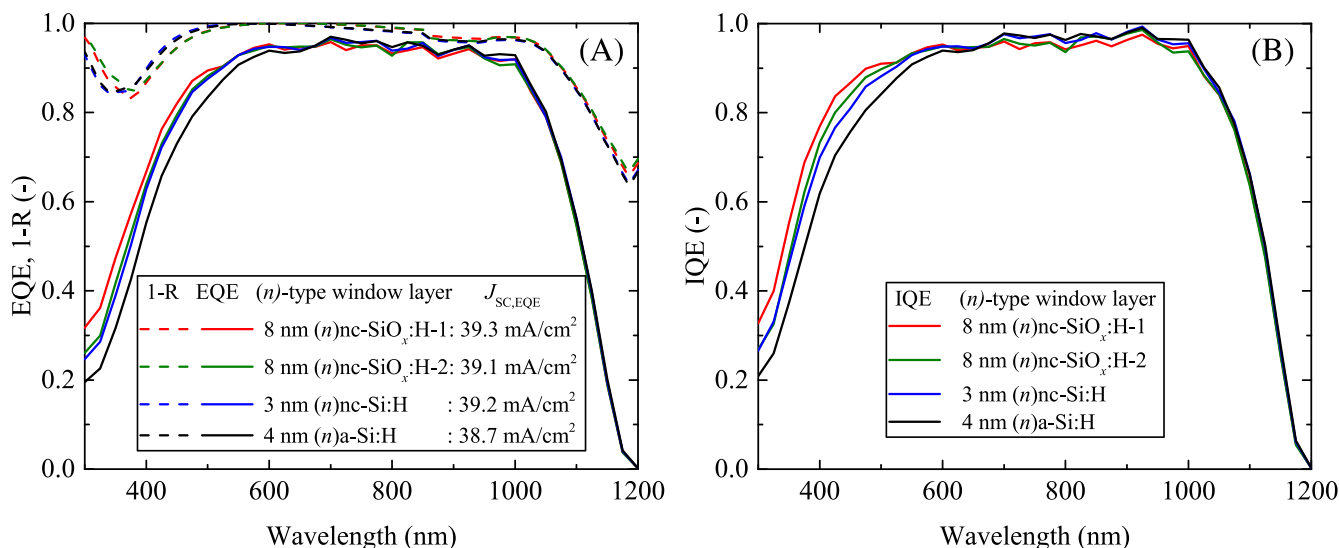


FIGURE 5 The (A) EQE, 1-R spectra, and (B) IQE spectra of rear junction FBC-SHJ cells with various (n)-contacts [Colour figure can be viewed at wileyonlinelibrary.com]

cells; (c) appearance of (n)c-Si/(i)a-Si:H and (n)-contact/ITO interfaces. The HRTEM images resulting from the front side interfaces of solar cells with 4-nm-thick (n)a-Si:H and 3-nm-thick (n)nc-Si:H are shown in Figure 6.

As illustrated in Figure 6A,B, together with recognizing ~ 6.5 -nm-thick (i)a-Si:H layer (see Figure S6), we confirm that the deposited thicknesses of (n)-contacts in the devices are close to the designated thicknesses, which are approximately 4 and 3 nm for (n)a-Si:H and (n)nc-Si:H, respectively. Besides, both (n)-contacts exhibit nearly fully amorphous microstructures. Although the (n)nc-Si:H layer appears amorphous, 1–3 nm crystalline seeds embedded in otherwise amorphous material cannot be excluded in the relatively thick TEM foil of about 20 nm. Typically, the amorphous incubation phase is around 2- to 3-nm-thick when the layer is deposited on (i)a-Si:H.⁶² As the (n)nc-

Si:H layer used in this study is only around 3 nm, it is difficult to observe any nanocrystalline phase in this 3-nm-thick (n)nc-Si:H layer. As the incubation phase is also part of the formation of (n)nc-Si:H layer, we still consider this 3-nm-thick layer to be (n)nc-Si:H or based on (n)nc-Si:H PECVD plasma growth conditions. Further advanced characterizations could help us to identify the eventual existence of nanocrystal in such a thin layer. For simplicity, we still name this 3-nm-thick layer as (n)nc-Si:H unless otherwise stated. Nevertheless, this (n)nc-Si:H layer exhibits different characteristics from the standard (n)a-Si:H. For the cell with (n)nc-Si:H, we observed a 1–2-nm-thick sublayer that is rougher than that of the (i)a-Si:H + (n)nc-Si:H bulk. This sublayer can be attributed to the formation of oxygen-rich (n)nc-Si:H/ITO interface as elaborated later in Figure 7A,B with EDX results. Besides, it is also worth noting that for the cell with

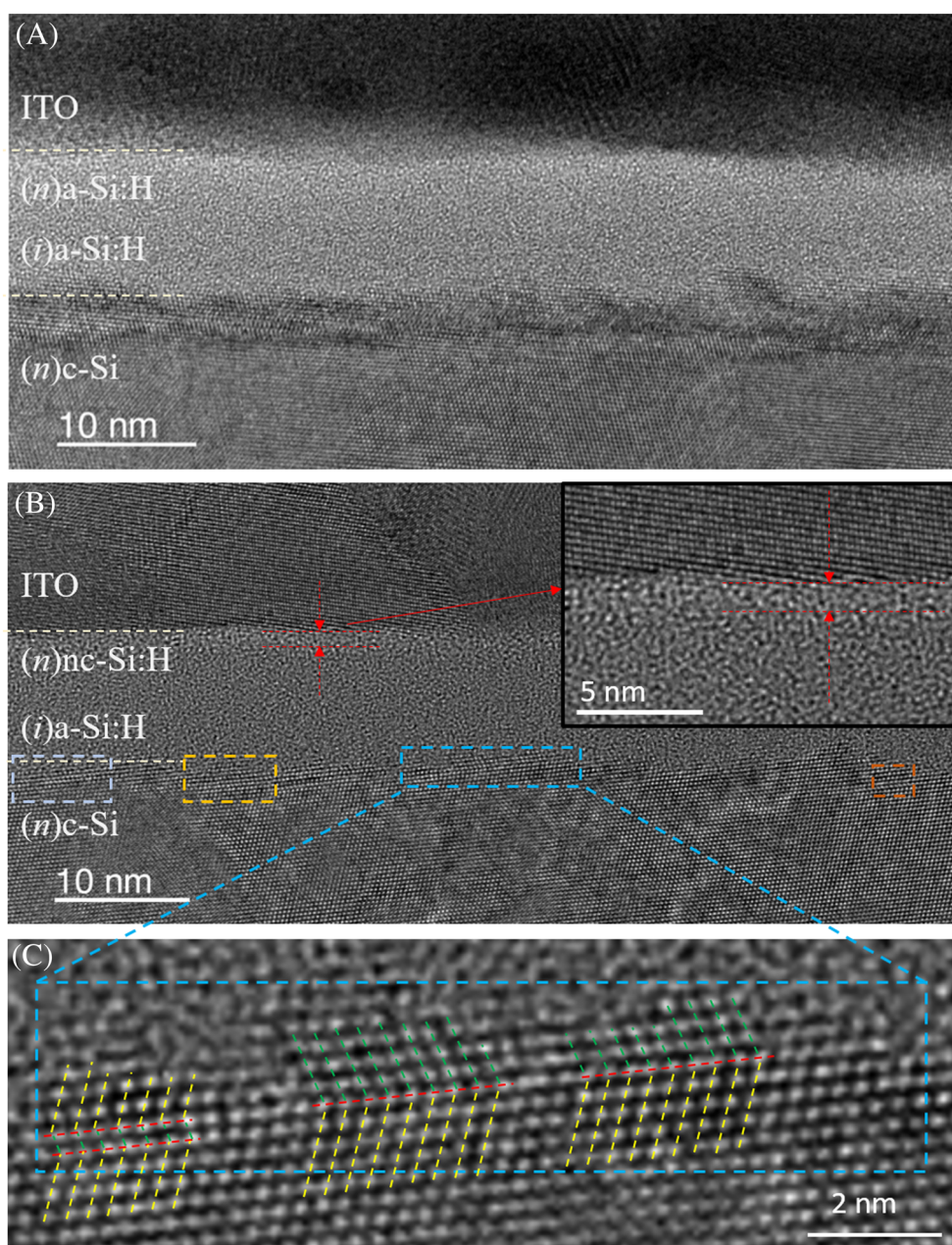


FIGURE 6 HRTEM cross-sectional images of FBC-SHJ solar cell's (n)-contact structures featuring (A) ~ 4 -nm-thick (n)a-Si:H, and (B) ~ 3 -nm-thick (n)nc-Si:H viewed from $\langle 110 \rangle$ orientation. The white dashed lines are guides to the eyes for distinguishing (n)nc-Si/(i)a-Si:H and (n)-contact/ITO interfaces. In Part (B), the red dashed lines and arrows highlight the 1–2 nm sublayer that is rougher than the (i)a-Si:H + (n)nc-Si:H bulk. The inset of Part (B) is the magnified region of the red dashed lines and arrows. The dashed colored rectangular areas include possible Si atoms double stacking faults and tiny twinned crystals with the c-Si wafer substrate. Part (C) exhibits the magnified dashed blue rectangle in Part (B). In Part (C), the dashed yellow lines represent the consistent Si atoms stacking with the c-Si wafer, the green dashed lines represent the Si atoms stackings with different orientations from the c-Si wafer [Colour figure can be viewed at wileyonlinelibrary.com]

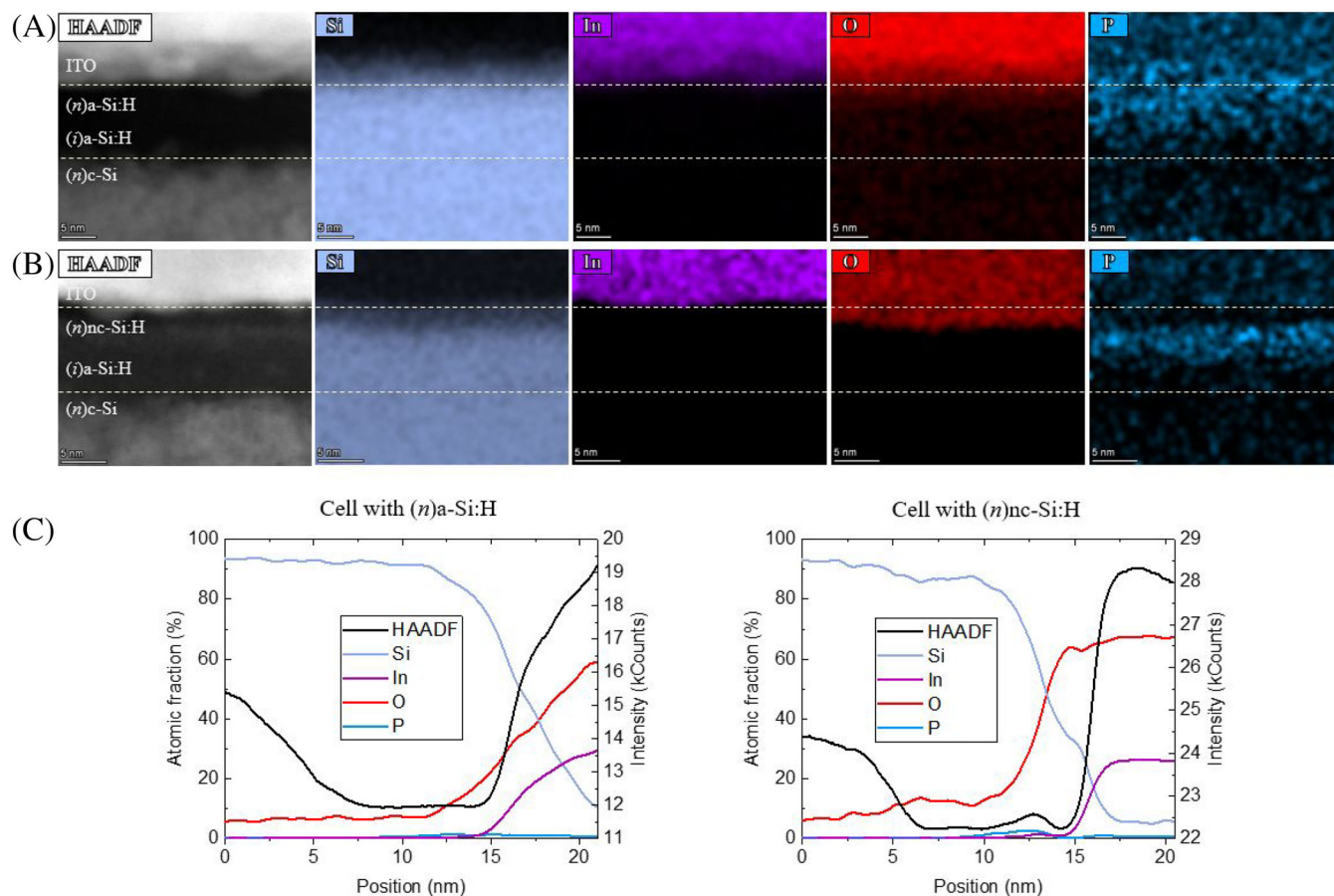


FIGURE 7 The scanning TEM (STEM) high-angle annular dark-field (HAADF) images combined with chemical compositional mapping measured by EDX of solar cells with (A) ~ 4 -nm-thick $(n)a$ -Si:H, and (B) ~ 3 -nm-thick $(n)nc$ -Si:H (n) -contacts. The white dashed lines are guides to the eyes for distinguishing $(n)c$ -Si/ $(i)a$ -Si:H and (n) -contact/ITO interfaces. Note that the P signal detected outside P-rich zones is an artifact, just as the O signal in the c-Si substrate. Part (C) presents the atomic fractions (intensity) of different elements (HAADF) for EDX mapping results that are shown in Parts (A) and (B). The “0-nm” position lies inside the $(n)c$ -Si wafer and it is close to the $(n)c$ -Si/ $(i)a$ -Si:H interface [Colour figure can be viewed at wileyonlinelibrary.com]

3-nm-thick $(n)nc$ -Si:H, on some occasions Si atoms double stacking faults and tiny twinned crystals on top of the c-Si substrate could be seen as shown in Figure 6C. A comprehensive study with similar observations was recently reported.⁶³ The formation of those crystals at c-Si/ $(i)a$ -Si:H interface could be induced by the highly hydrogen-diluted plasma and the lack of oxygen during the deposition.^{52,64,65} For those reasons, unlike $(n)nc$ -Si:H, we hardly observed those crystalline structures at c-Si/ $(i)a$ -Si:H interface for both cells with $(n)a$ -Si:H and $(n)nc$ -SiO_x-H-1 (see Figure S6).

As shown in the O maps of Figure 7A,B, we observed more oxygen presence in/near the P-rich region of the 3-nm-thick $(n)nc$ -Si:H as compared to the $(n)a$ -Si:H counterparts. Further, from the Si map, we can also identify a reduced Si atomic fraction of deposited $(n)nc$ -Si:H close to ITO, while $(n)a$ -Si:H remains a similar atomic percentage of Si as compared to that of the $(i)a$ -Si:H beneath. Similar observations of reduced Si atomic fraction and prominent O incorporation are also found for $(n)nc$ -SiO_x-H-1 (see Figure S6). Therefore, both O and Si maps of the cell with $(n)nc$ -Si:H indicate significant amounts of oxygen incorporations into the deposited $(n)nc$ -Si:H. The more numerous

oxygen incorporations can be ascribed to the possibly more porous phase of $(n)nc$ -Si:H as it is close to the intermediate highly porous amorphous-to-crystalline transition phase.⁶⁶ This finding suggests a possible less resistive $(n)a$ -Si:H/ITO interface as compared to $(n)nc$ -Si:H/ITO interface, which may explain the slightly higher FF observed for the cell with $(n)a$ -Si:H aside from the fact that 4-nm-thick $(n)a$ -Si:H is more conductive than 3-nm-thick $(n)nc$ -Si:H (see Figure 4). Similar observations were also reported by Sheng et al., who conducted X-ray photoelectron spectroscopy (XPS) depth profiling measurements on (n) -type layer/ITO interface for amorphous silicon solar cells.⁶⁷ The $(n)a$ -Si:H/ITO interface exhibited advantageous characteristics as compared to that of $(n)\mu c$ -Si:H, such as lack of oxygen segregation, less oxidized Si thin films around the interface region, and less ITO in-diffusion. While as seen in our EDX results, indium (In) is well constrained within ITO for all (n) -contacts investigated. Lastly, due to the very tiny atomic fractions and large scatterings of P content in all samples, we cannot justify if there is any statistical difference in P content from those EDX results between the two samples, though a near-zero P content in the oxygen-rich $(n)nc$ -Si:H layer can be concluded from

the EDX results. Further investigations are needed for a more complete comparison between the (active) doping concentrations in the various thin (*n*)-contacts.

3.4 | Solar cells—Effects of interface treatments

To mitigate the possible resistive interface of (*n*)nc-Si:H with ITO as observed in Figure 7, we deposited 2-nm (*n*)a-Si:H capping layer on top of the 3-nm-thick (*n*)nc-Si:H. This extra (*n*)a-Si:H aims at improving the transport of electrons through (*n*)a-Si:H/ITO interface. Besides, the effects of HPT + VHF (*i*)nc-Si:H treatments, which were already applied for solar cells with 3-nm-thick (*n*)nc-Si:H (*n*)-contact in Figure 4, are also investigated in this section. Note that we have not observed any detectable layer growth or etching by SE after 6 minutes of VHF (*i*)nc-Si:H deposition. The *J*-*V* parameters of solar cells are shown in Figure 8.

As presented in Figure 8, the combined HPT + VHF (*i*)nc-Si:H treatments significantly improved *i*- V_{OC} of precursors (before ITO) from 734 to 745 mV. Aside from an 11-mV gain of cells' V_{OC} , we also observed a slightly increased J_{SC} and a nearly 3%_{abs.} *FF* improvement by applying the treatments. Those improvements are related to more hydrogen incorporation induced by the treatments, which improve the passivation quality and increase the bandgap of (*i*)a-Si:H layers.³⁸ Nevertheless, the additional 2 nm of (*n*)a-Si:H capping layer further improved the *FF* to 80%, which could partially be attributed to a better (*n*)a-Si:H/ITO interface as expected from the EDX results and also a more conductive (*n*)-contact stack as discussed in Section 3.1. Although we observed a slightly lower *i*- V_{OC} already before ITO

deposition when (*n*)a-Si:H capping layer was applied, the precursor preserved its passivation quality after ITO sputtering, unlike passivation degradations observed for other (*n*)nc-Si:H single-layer counterparts. Nevertheless, mainly due to extra parasitic absorption that was induced by this additional (*n*)a-Si:H layer, cells exhibited 0.4%_{abs.} lower efficiency as compared to the cells with only the combined HPT and VHF (*i*)nc-Si:H treatments. Overall, 3-nm-thick (*n*)nc-Si:H with combined HPT + VHF (*i*)nc-Si:H treatments is appealing to be used as the window layer mainly thanks to the high J_{SC} and the promising *FF* of the cells.

3.5 | Solar cells—Certified *I*-*V* and MgF₂/ITO double-layer anti-reflection coating

The best cell with 3-nm-thick (*n*)nc-Si:H and the reference cell with 4-nm-thick (*n*)a-Si:H were chosen to be independently certified at ISFH CalTec (Hamelin, Germany). Both cells feature the same layer stacks and fabrication process except for the (*n*)-contact. The measured *I*-*V* parameters are shown in Figure 9. The cell with 3-nm-thick (*n*)nc-Si:H exhibits certified designated area η of 22.20%, which is 0.44%_{abs.} higher than that of (*n*)a-Si:H counterparts mainly due to the highly transparent thin (*n*)nc-Si:H window layer. As reported previously,^{19,22} for doped layers thicker than ~ 9 nm, J_{SC} gains were observed for cells with doped nc-Si:H rather than for cells with a-Si:H with comparable thicknesses. Here, we exploit further the more optical advantageous (*n*)nc-Si:H over the (*n*)a-Si:H at an ultra-thin thickness level (~ 3 to 4 nm). Nevertheless, further comprehensive studies including fine-tuning of our processes are needed to draw more

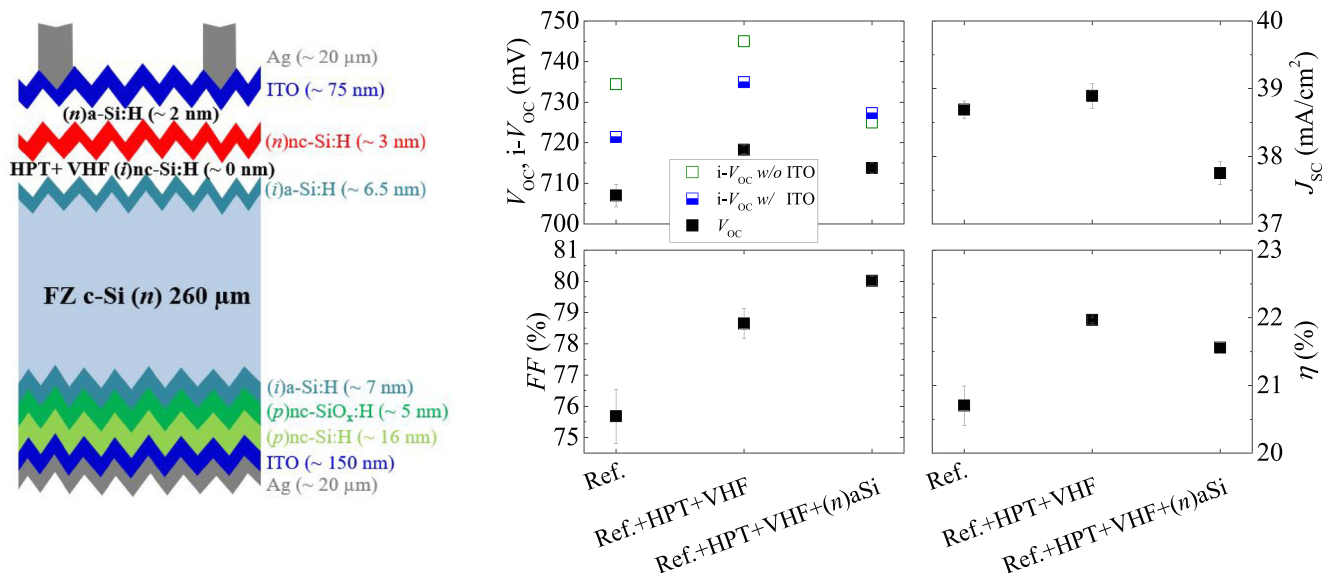


FIGURE 8 The schematic sketches and external parameters of rear junction FBC-SHJ cells featuring 3-nm-thick (*n*)nc-Si:H as (*n*)-type contact as function of HPT + VHF (*i*)nc-Si:H and (*n*)a-Si:H capping layer treatments. Solar cells without any treatment are denoted as the reference (Ref.). The VHF (*i*)nc-Si:H is abbreviated as VHF. Note that we have not observed any detectable layer growth or etching by SE after 6 minutes of VHF (*i*)nc-Si:H deposition. The results represent averaged parameters with four solar cells (3.92 cm²) and the error bars represent the standard deviations [Colour figure can be viewed at wileyonlinelibrary.com]

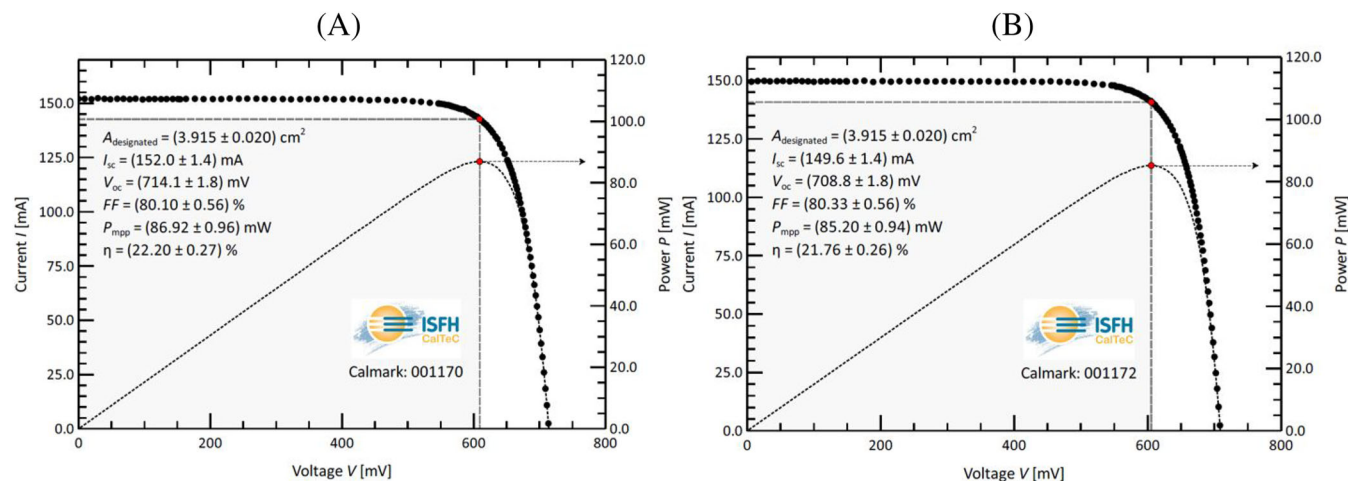


FIGURE 9 The independently certified I - V characteristics and device parameters of the best rear junction FBC-SHJ solar cells featuring (A) 3-nm-thick $(n)nc$ -Si:H and (B) 4-nm-thick $(n)a$ -Si:H contact. Both cells feature the same layer stacks and fabrication process except for the (n) -contact. The certifications were performed at ISFH CalTeC (Hamelin, Germany) [Colour figure can be viewed at wileyonlinelibrary.com]

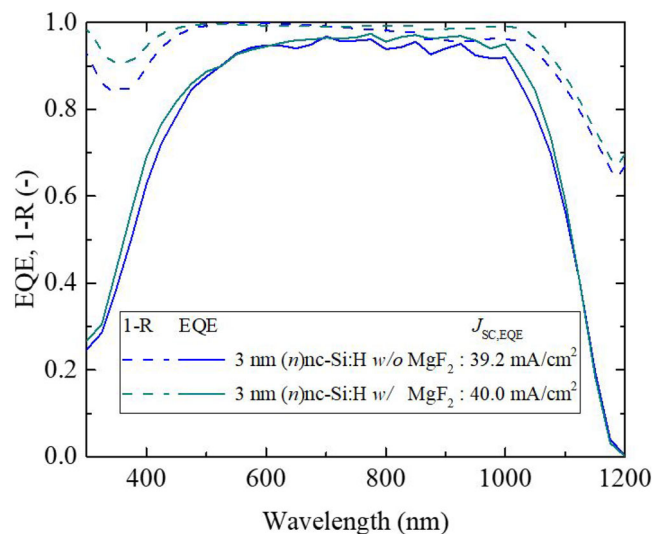


FIGURE 10 The EQE and 1-R spectra of rear junction FBC-SHJ cell featuring 3-nm-thick $(n)nc$ -Si:H with and without MgF_2 for forming DLARC with ITO [Colour figure can be viewed at wileyonlinelibrary.com]

detailed conclusions. It is worth noting that our screen-printed Ag front fingers feature a designated width of ~ 70 μm , which leaves still plenty of room for improving further the J_{SC} of the solar cells. Nevertheless, our 3 nm thin $(n)nc$ -Si:H enabling efficiency above 22% is thinner than the state-of-art minimum required thickness for $(n)nc$ -Si:H or $(n)nc$ -SiO_x:H-based (n) -contacts for high-efficiency SHJ solar cells,^{16,19,22,28} thus enabling lower material consumptions and potentials for higher industrial throughputs.

To further explore the potential of the optimized stack, we applied an additional 100-nm-thick MgF_2 layer on top of the ITO to form the double-layer anti-reflection coating (DLARC).^{68,69} We demonstrate a $J_{SC,EQE}$ up to 40.0 mA/cm^2 for the cell with 3-nm-thick (n)

nc -Si:H as shown in Figure 10. This $J_{SC,EQE}$ gain brings the active area η_{active} to 22.88% and originates from the better anti-reflection effects induced by the DLARC. Thus, we observed 0.2 and 0.6 mA/cm^2 $J_{SC,EQE}$ improvements in the wavelength ranges below and above 600 nm, respectively. Further improvements to achieve cell $\eta > 23\%$ in the short-term are (a) a more transparent TCO, such as IFO:H,⁷⁰ (b) a lower front metal coverage via finer-line screen printing or copper-plating,⁷¹ and (c) a better passivation quality by applying a bilayer $(i)a$ -Si:H layer stack.^{63,72}

4 | CONCLUSIONS

In this work, aiming at minimizing the parasitic absorptions induced by (n) -type window layers, we studied opto-electrical properties of $(n)a$ -Si:H, two types of $(n)nc$ -SiO_x:H, and $(n)nc$ -Si:H layers and implement them (as thin as 2 nm) into rear junction FBC-SHJ solar cells.

We firstly investigated and compared various (n) -type layers both optically and electrically, where $(n)a$ -Si:H is the least optical favorable then followed by $(n)nc$ -Si:H and two $(n)nc$ -SiO_x:H layers. However, due to the observed thickness- and substrate-dependent electrical properties, nc -Si:H-based layers exhibited lower σ_{dark} and generally higher E_a values than that of $(n)a$ -Si:H when they were deposited on $(i)a$ -Si:H coated glasses with thicknesses below 20 nm. Accordingly, those layers were integrated into rear junction FBC-SHJ solar cells. We noticed a strong correlation between (n) -contacts properties and cell precursors' passivation qualities after ITO sputtering. That is, a thicker and a more conductive (n) -contact tends to exhibit a higher passivation resilience to ITO sputtering and a smaller gap from i - V_{OC} to V_{OC} . Besides, we also found that (n) -layer with a higher E_{O4} or a larger σ_{dark} (lower E_a) delivers a higher J_{SC} or a higher FF in well-passivated solar cells ($V_{OC} > 710$ mV), respectively.

Subsequently from HRTEM and EDX analysis, a higher oxygen presence near (n)nc-Si:H/ITO interface is revealed as compared to the (n)a-Si:H counterpart, which suggests a less resistive (n)a-Si:H/ITO interface and thus contributing to slightly higher FFs observed in solar cells. Eventually, we demonstrated the successful application of an ultra-thin layer of only 3-nm-thick based on (n)nc-Si:H PECVD plasma growth conditions together with HPT + VHF (i)nc-Si:H that delivers a certified designated area η of 22.20%. This cell shows 0.61 mA/cm² J_{SC} gain over the (n)a-Si:H counterpart owing to the higher transparency of (n)nc-Si:H, while maintaining comparable $V_{OC} > 714$ mV and $FF > 80\%$. Further, the cell with 3-nm-thick (n)nc-Si:H featuring MgF₂/ITO DLARC exhibits a $J_{SC,EQE}$ of 40.0 mA/cm² and an active area η_{active} of 22.88%.

ACKNOWLEDGEMENTS

This study receives financial support from the NWO Joint Solar Program III (680-91-011) and technical support from PVMD group technicians Martijn Tijssen, Stefaan Heirman, and Daragh O'Connor.

CONFLICT OF INTEREST

The authors declare that they have no known competing financial interests or personal relationships that could have appeared to influence the work reported in this paper.

DATA AVAILABILITY STATEMENT

The data that support the findings of this study are available from the corresponding author upon reasonable request.

ORCID

Yifeng Zhao  <https://orcid.org/0000-0003-3789-5090>

Paul Procel  <https://orcid.org/0000-0003-4997-3551>

Can Han  <https://orcid.org/0000-0002-3213-6856>

REFERENCES

- Adachi D, Hernández JL, Yamamoto K. Impact of carrier recombination on fill factor for large area heterojunction crystalline silicon solar cell with 25.1% efficiency. *Appl Phys Lett*. 2015;107(23):233506.
- Mazzarella L, Morales-Vilches AB, Hendrichs M, et al. Nanocrystalline n-type silicon oxide front contacts for silicon heterojunction solar cells: photocurrent enhancement on planar and textured substrates. *IEEE J Photovoltaics*. 2018;8(1):70-78.
- Zhao Y, Mazzarella L, Procel P, et al. Doped hydrogenated nanocrystalline silicon oxide layers for high-efficiency c-Si heterojunction solar cells. *Prog Photovolt Res Appl*. 2020;28(5):425-435.
- Cuony P, Alexander DTL, Perez-Wurfl I, et al. Silicon filaments in silicon oxide for next-generation photovoltaics. *Adv Mater*. 2012;24(9):1182-1186.
- Mazzarella L, Kirner S, Stannowski B, Korte L, Rech B, Schlatmann R. p-type microcrystalline silicon oxide emitter for silicon heterojunction solar cells allowing current densities above 40 mA/cm². *Appl Phys Lett*. 2015;106(2):23902.
- Richter A, Smirnov V, Lambert A, Nomoto K, Welter K, Ding K. Versatility of doped nanocrystalline silicon oxide for applications in silicon thin-film and heterojunction solar cells. *Sol Energy Mater Sol Cells*. 2018;174:196-201.
- Morales-Vilches AB, Mazzarella L, Hendrichs M, et al. Nanocrystalline vs. amorphous n-type silicon front surface field layers in silicon heterojunction solar cells: role of thickness and oxygen content. *33rd Eur. Photovolt. Sol. Energy Conf. Exhib*. 2017;715-719.
- Martins R, Macarico A, Ferreira I, et al. Highly conductive and highly transparent n-type microcrystalline silicon thin films. *Thin Solid Films*. 1997;303(1-2):47-52.
- Ru X, Qu M, Wang J, et al. 25.11% efficiency silicon heterojunction solar cell with low deposition rate intrinsic amorphous silicon buffer layers. *Sol Energy Mater Sol Cells*. 2020;215:110643.
- Kebblinski P, Phillpot SR, Wolf D, Gleiter H. Amorphous structure of grain boundaries and grain junctions in nanocrystalline silicon by molecular-dynamics simulation. *Acta Mater*. 1997;45(3):987-998.
- Monroy BM, Remolina Millán A, Garcia-Sanchez MF, et al. Structure and optical properties of silicon nanocrystals embedded in amorphous silicon thin films obtained by PECVD. *J Nanomater*. 2011;2011:1-9.
- Roca i Cabarrocas P, Layadi N, Heitz T, Drévillon B, Solomon I. Substrate selectivity in the formation of microcrystalline silicon: mechanisms and technological consequences. *Appl Phys Lett*. 1995;66(26):3609-3611.
- Kondo M, Toyoshima Y, Matsuda A, Ikuta K. Substrate dependence of initial growth of microcrystalline silicon in plasma-enhanced chemical vapor deposition. *J Appl Phys*. 1996;80(10):6061-6063.
- Pellaton Vaucher N, Rech B, Fischer D, et al. Controlled nucleation of thin microcrystalline layers for the recombination junction in a-Si stacked cells. *Sol Energy Mater Sol Cells*. 1997;49(1-4):27-33.
- Mazzarella L, Kirner S, Gabriel O, et al. Nanocrystalline silicon emitter optimization for Si-HJ solar cells: substrate selectivity and CO₂ plasma treatment effect. *Phys Status Solidi Appl Mater Sci*. 2017;214(2):1532958.
- Mazzarella L, Morales-Vilches AB, Korte L, Schlatmann R, Stannowski B. Ultra-thin nanocrystalline n-type silicon oxide front contact layers for rear-emitter silicon heterojunction solar cells. *Sol Energy Mater Sol Cells*. 2018;179:386-391.
- Wolff J, Carius R, Finger F. Preparation of microcrystalline silicon seed-layers with defined structural properties. *Thin Solid Films*. 2003;427(1-2):46-50.
- Zhou J, Ikuta K, Yasuda T, et al. Growth of amorphous-layer-free microcrystalline silicon on insulating glass substrates by plasma-enhanced chemical vapor deposition. *Appl Phys Lett*. 2003;1534(1997):1-4.
- Nogay G, Seif JP, Riesen Y, et al. Nanocrystalline silicon carrier collectors for silicon heterojunction solar cells and impact on low-temperature device characteristics. *IEEE J Photovoltaics*. 2016;6(6):1654-1662.
- Watahiki T, Furuhashi T, Matsuura T, et al. Rear-emitter Si heterojunction solar cells with over 23% efficiency. *Appl Phys Express*. 2015;8(2):021402.
- Finger F, Hapke P, Luysberg M, Carius R, Wagner H, Scheib M. Improvement of grain size and deposition rate of microcrystalline silicon by use of very high frequency glow discharge. *Appl Phys Lett*. 1994;65(20):2588-2590.
- Seif JP, Descoedres A, Nogay G, et al. Strategies for doped nanocrystalline silicon integration in silicon heterojunction solar cells. *IEEE J Photovoltaics*. 2016;6(5):1132-1140.
- Lei C, Peng C-W, Zhong J, et al. Phosphorus treatment to promote crystallinity of the microcrystalline silicon front contact layers for highly efficient heterojunction solar cells. *Sol Energy Mater Sol Cells*. 2020;209:110439.
- Koh J, Fujiwara H, Koval RJ, Wronski CR, Collins RW. Real time spectroscopic ellipsometry studies of the nucleation and growth of p-type microcrystalline silicon films on amorphous silicon using B₂H₆, B(CH₃)₃ and BF₃ dopant source gases. *J Appl Phys*. 1999;85(8):4141-4153.
- Pangal K, Sturm JC, Wagner S, Büyüklımanlı TH. Hydrogen plasma enhanced crystallization of hydrogenated amorphous silicon films. *J Appl Phys*. 1999;85(3):1900-1906.

26. Zhou HP, Xu M, Xu S, et al. Hydrogen-plasma-induced rapid, low-temperature crystallization of μm -thick a-Si: H films. *Sci Rep*. 2016; 6(1):1-8.
27. Procel P, Yang G, Isabella O, Zeman M. Theoretical evaluation of contact stack for high efficiency IBC-SHJ solar cells. *Sol Energy Mater Sol Cells*. 2018;186:66-77.
28. Qiu D, Duan W, Lambertz A, et al. Front contact optimization for rear-junction SHJ solar cells with ultra-thin n-type nanocrystalline silicon oxide. *Sol Energy Mater Sol Cells*. 2020;209: 110471.
29. Phong D, Kim S, Kim S, et al. Materials science in semiconductor processing ultra-thin stack of n-type hydrogenated microcrystalline silicon and silicon oxide front contact layer for rear-emitter silicon heterojunction solar cells. *Mater Sci Semicond Process*. 2019;96(October 2018):1-7.
30. Zhao Y, Procel P, Han C, et al. Design and optimization of hole collectors based on nc-SiOx: H for high-efficiency silicon heterojunction solar cells. *Sol Energy Mater Sol Cells*. 2021;219:110779.
31. Yang G, Guo P, Procel P, et al. High-efficiency black IBC c-Si solar cells with poly-Si as carrier-selective passivating contacts. *Sol Energy Mater Sol Cells*. 2018;186:9-13.
32. Santbergen R, Meguro T, Suezaki T, Koizumi G, Yamamoto K, Zeman M. GenPro4 optical model for solar cell simulation and its application to multijunction solar cells. *IEEE J Photovoltaics*. 2017;7(3): 919-926.
33. Bailly M, Carpenter J V, Holman Z, Bowden S. Substrate dependent growth of microcrystalline silicon. *2014 IEEE 40th Photovolt. Spec. Conf*. 2014;1201-1205.
34. Wernerus H, Bivour M, Kroely L, Hermle M, Wolke W. Characterization of ultra-thin μc -Si: H films for silicon heterojunction solar cells. *Energy Procedia*. 2014;55:310-319.
35. Ast DG, Brodsky MH. Thickness and temperature dependence of the conductivity of phosphorus-doped hydrogenated amorphous silicon. *Philos Mag B*. 1980;41(3):273-285.
36. Hasegawa S, Shimizu S, Kurata Y. Thickness dependences of properties of P- and B-doped hydrogenated amorphous silicon: II. ESR, hydrogen vibrational spectra and optical absorption. *Philos Mag B*. 1984;49(5):521-532.
37. Matsumoto T, Suzuki J, Ohnuma M, Kanemitsu Y, Masumoto Y. Evidence of quantum size effect in nanocrystalline silicon by optical absorption. *Phys Rev B*. 2001;63(19):195322.
38. Descoedres A, Barraud L, De Wolf S, et al. Improved amorphous/crystalline silicon interface passivation by hydrogen plasma treatment. *Appl Phys Lett*. 2011;99(12):1-4.
39. Knights JC, Street RA, Lucovsky G. Electronic and structural properties of plasma-deposited a-Si: O: H—the story of O₂. *J Non-Cryst Solids*. 1980;35:279-284.
40. Parker JH Jr, Feldman DW, Ashkin M. Raman scattering by silicon and germanium. *Phys Rev*. 1967;155(3):712-714.
41. Richter H, Wang ZP, Ley L. The one phonon Raman spectrum in microcrystalline silicon. *Solid State Commun*. 1981; 39(5):625-629.
42. Campbell IH, Fauchet PM. The effects of microcrystal size and shape on the one phonon Raman spectra of crystalline semiconductors. *Solid State Commun*. 1986;58(10):739-741.
43. Zi J, Büscher H, Falter C, Ludwig W, Zhang K, Xie X. Raman shifts in Si nanocrystals. *Appl Phys Lett*. 1996;69(2):200-202.
44. Wei W, Xu G, Wang J, Wang T. Raman spectra of intrinsic and doped hydrogenated nanocrystalline silicon films. *Vacuum*. 2007;81(5): 656-662.
45. Iqbal Z, Veprek S. Raman scattering from hydrogenated microcrystalline and amorphous silicon. *J Phys C Solid State Phys*. 1982;15(2): 377-392.
46. Spear WE, Le Comber PG. Substitutional doping of amorphous silicon. *Solid State Commun*. 1975;17(9):1193-1196.
47. Rehm W, Fischer R, Stuke J, Wagner H. Photo and dark conductivity of doped amorphous silicon. *Phys Status Solidi*. 1977;79(2):539-547.
48. Kaya H, Imura T, Kusao T, et al. Evaluation of boron and phosphorus doping microcrystalline silicon films. *Jpn J Appl Phys*. 1984;23(8A): L549-L551.
49. Guha S, Yang J, Nath P, Hack M. Enhancement of open circuit voltage in high efficiency amorphous silicon alloy solar cells. *Appl Phys Lett*. 1986;49(4):218-219.
50. Wang S, Smirnov V, Chen T, et al. Effects of oxygen incorporation in solar cells with a-SiOx: H absorber layer. *Jpn J Appl Phys*. 2014;54(1): 011401.
51. Tan H, Babal P, Zeman M, Smets AHM. Wide bandgap p-type nanocrystalline silicon oxide as window layer for high performance thin-film silicon multi-junction solar cells. *Sol Energy Mater Sol Cells*. 2015; 132:597-605.
52. Lambertz A, Grundler T, Finger F. Hydrogenated amorphous silicon oxide containing a microcrystalline silicon phase and usage as an intermediate reflector in thin-film silicon solar cells. *J Appl Phys*. 2011; 109(11):113109.
53. Richter A, Zhao L, Finger F, Ding K. Nano-composite microstructure model for the classification of hydrogenated nanocrystalline silicon oxide thin films. *Surf Coat Technol*. 2016;295:119-124.
54. Cuony P, Marending M, Alexander DTL, et al. Mixed-phase p-type silicon oxide containing silicon nanocrystals and its role in thin-film silicon solar cells. *Appl Phys Lett*. 2010;97(21):213502.
55. Umishio H, Sai H, Koida T, Matsui T. Nanocrystalline-silicon hole contact layers enabling efficiency improvement of silicon heterojunction solar cells: impact of nanostructure evolution on solar cell performance. *Prog Photovolt Res Appl*. 2021;29(3):344-356.
56. Chang K-J, Chadi DJ. Theory of hydrogen passivation of shallow-level dopants in crystalline silicon. *Phys Rev Lett*. 1988;60(14):1422-1425.
57. Johnson NM, Herring C, Chadi DJ. Interstitial hydrogen and neutralization of shallow-donor impurities in single-crystal silicon. *Phys Rev Lett*. 1986;56(7):769-772.
58. Bergman K, Stavola M, Pearson SJ, Lopata J. Donor-hydrogen complexes in passivated silicon. *Phys Rev B*. 1988;37(5):2770-2773.
59. Mercaldo LV, Bobeico E, Usatii I, et al. Potentials of mixed-phase doped layers in p-type Si heterojunction solar cells with ZnO: Al. *Sol Energy Mater Sol Cells*. 2017;169:113-121.
60. Kirner S, Mazzarella L, Korte L, Stannowski B, Rech B, Schlatmann R. Silicon heterojunction solar cells with nanocrystalline silicon oxide emitter: insights into charge carrier transport. *IEEE J Photovoltaics*. 2015;5(6):1601-1605.
61. Procel P, Xu H, Saez A, et al. The role of heterointerfaces and subgap energy states on transport mechanisms in silicon heterojunction solar cells. *Prog Photovolt Res Appl*. 2020;28(9):935-945.
62. Tomasi A, Paviet-Salomon B, Jeangros Q, et al. Simple processing of back-contacted silicon heterojunction solar cells using selective-area crystalline growth. *Nat Energy*. 2017;2(5):1-8.
63. Qu X, He Y, Qu M, et al. Identification of embedded nanotwins at c-Si/a-Si:H interface limiting the performance of high-efficiency silicon heterojunction solar cells. *Nat Energy*. 2021;1-9.
64. Matsuda A. Formation kinetics and control of microcrystallite in μc -Si: H from glow discharge plasma. *J Non-Cryst Solids*. 1983;59-60: 767-774.
65. Geissbühler J, De Wolf S, Demareux B, et al. Amorphous/crystalline silicon interface defects induced by hydrogen plasma treatments. *Appl Phys Lett*. 2013;102(23):231604.
66. Roca i Cabarrocas P, Layadi N, Drevillon B, Solomon I. Microcrystalline silicon growth by the layer-by-layer technique: long term evolution and nucleation mechanisms. *J Non-Cryst Solids*. 1996;198-200: 871-874.
67. Sheng S, Hao H, Diao H, et al. XPS depth profiling study of n/TCO interfaces for p-i-n amorphous silicon solar cells. *Appl Surf Sci*. 2006; 253(3):1677-1682.

68. Zhang D, Digdaya IA, Santbergen R, et al. Design and fabrication of a SiO_x/ITO double-layer anti-reflective coating for heterojunction silicon solar cells. *Sol Energy Mater Sol Cells*. 2013;117:132-138.
69. Han C, Zhao Y, Mazzarella L, et al. Room-temperature sputtered tungsten-doped indium oxide for improved current in silicon heterojunction solar cells. *Sol Energy Mater Sol Cells*. 2021;227:111082.
70. Han C, Mazzarella L, Zhao Y, et al. High-mobility hydrogenated fluorine-doped indium oxide film for passivating contacts c-Si solar cells. *ACS Appl Mater Interfaces*. 2019;11(49):45586-45595.
71. Yu J, Li J, Zhao Y, et al. Copper metallization of electrodes for silicon heterojunction solar cells: process, reliability and challenges. *Sol Energy Mater Sol Cells*. 2021;224:110993.
72. Sai H, Chen P-W, Hsu H-J, et al. Impact of intrinsic amorphous silicon bilayers in silicon heterojunction solar cells. *J Appl Phys*. 2018;124(10):103102.

SUPPORTING INFORMATION

Additional supporting information may be found in the online version of the article at the publisher's website.

How to cite this article: Zhao Y, Mazzarella L, Procel P, et al. Ultra-thin electron collectors based on nc-Si:H for high-efficiency silicon heterojunction solar cells. *Prog Photovolt Res Appl*. 2021;1-14. doi:10.1002/pip.3502